Article

Enabling Stable Interphases via In Situ Two-Step Synthetic Bilayer Polymer Electrolyte for Solid-State Lithium Metal Batteries

Ying Liu, Fang Fu, Chen Sun, Aotian Zhang, Hong Teng, Liqun Sun * and Haiming Xie *

National & Local United Engineering Laboratory for Power Battery, Department of Chemistry, Northeast Normal University, Changchun 130024, China; liuy693@nenu.edu.cn (Y.L.); fuf558@nenu.edu.cn (F.F.); sunc243@nenu.edu.cn (C.S.); zhangat266@nenu.edu.cn (A.Z.); tengh466@nenu.edu.cn (H.T.)
* Correspondence: sunlq446@nenu.edu.cn (L.S.); xiehm136@nenu.edu.cn (H.X.)

Abstract: Poly(ethylene oxide) (PEO)-based electrolyte is considered to be one of the most promising polymer electrolytes for lithium metal batteries. However, a narrow electrochemical stability window and poor compatibility at electrode-electrolyte interfaces restrict the applications of PEO-based electrolyte. An in situ synthetic double-layer polymer electrolyte (DLPE) with polyacrylonitrile (PAN) layer and PEO layer was designed to achieve a stable interface and application in high-energy-density batteries. In this special design, the hydroxy group of PEO-SPE can form an O-H—N hydrogen bond with the cyano group in PAN-SPE, which connects the two layers of DLPE at a microscopic chemical level. A special Li$^+$ conducting mechanism in DLPE provides a uniform Li$^+$ flux and fast Li$^+$ conduction, which achieves a stable electrolyte/electrode interface. LiFePO$_4$/DLPE/Li battery shows superior cycling stability, and the coulombic efficiency remains 99.5% at 0.2 C. Meanwhile, LiNi$_{0.6}$Co$_{0.2}$Mn$_{0.2}$O$_2$/DLPE/Li battery shows high specific discharge capacity of 176.0 mAh g^{-1} at 0.1 C between 2.8 V to 4.3 V, and the coulombic efficiency remains 95% after 100 cycles. This in situ synthetic strategy represents a big step forward in addressing the interface issues and boosting the development of high-energy-density lithium-metal batteries.

Keywords: solid-state lithium metal battery; solid polymer electrolyte; double-layer electrolyte; interfacial stability

1. Introduction

There has been a global effort to develop next-generation energy storage systems to meet the demanding requirements of electric vehicles and grid-scale energy storage [1,2]. Lithium-ion batteries (LIBs) play an indispensable role in energy storage systems due to their mature technology, low cost, and high coulombic efficiency [3,4]. However, state-of-the-art LIBs with a graphite anode have almost reached the theoretical energy density of 350–400 Wh kg^{-1}, which cannot match the increasing demand of advanced electronic devices [5,6]. To obtain high energy density batteries, using Li metal anodes (LMBs) is a promising approach, owing to their high theoretical capacity (3860 mAh g^{-1}) and low electrochemical potential (−3.04 V vs. standard hydrogen electrodes) [7,8]. Nevertheless, most LMBs using flammable organic liquid electrolytes have the serious issues of short circuit and leakage, which may cause a fire hazard that can lead to an explosion [9,10]. This is due to the side reaction of Li metal and electrolytes, which creates an instability interface between the anode and the electrolyte that generates lithium dendrites and produces by-product gas that leads to battery swelling and deformation [11,12]. Compared with liquid electrolytes, solid polymer electrolytes (SPE), with high thermal and chemical stability and high Young's modulus, that can resist the growth of lithium dendrites may be a good choice to address these safety issues [13,14].

Among the prevalent SPE, the poly(ethylene oxide) (PEO)-based electrolyte is the most extensively studied electrolyte [15]. This may be attributed to the excellent flexibility and good membrane-forming merits of PEO [16,17]. Owing to the anodic stability, PEO is often used in lithium metal batteries, such as the matrix of single ion conduction or buffer layers [18,19]. However, the electrochemical stability window of PEO is fairly narrow, as it is easily oxidized to ethers at voltages above 3.9 V [20]. Moreover, recent studies have shown that the cathode can accelerate the oxidation of PEO under the high voltage of 4.2 V [21]. These shortcomings limit the matching of PEO-based electrolytes with high voltage transition metal cathodes and hinder the development of high-energy-density batteries. To tackle these problems, many efforts have been made to design novel solid-state electrolytes (SSEs) and to form stable electrolyte-electrode interfaces [22,23]. A novel idea is to construct a multilayered solid electrolyte [24,25]. The multilayered structure is compatible with high voltage cathodes and is stable when used with lithium metal anodes, making it suitable for use with high-voltage lithium metal batteries [26]. However, as the number of electrolyte layers increases, new interfaces are introduced, and the impedance of the battery will increase accordingly [27].

In this paper, we propose a double-layer polymer electrolyte (DLPE) produced by an in situ two-step synthetic method. The first step involves the formation of polyacrylonitrile (PAN)-SPE on the cathode and the second involves the cross-linking of PEO-SPE on PAN-SPE. This in situ synthetic method contributes to creating an intimate contact at the electrode-electrolyte and electrolyte-electrolyte interfaces. More importantly, once PEO contacts with PAN, the hydroxy group of PEO-SPE can form an O-H⁻N hydrogen bond with the cyano group in PAN-SPE, which connects the two layers of DLPE at a microscopic chemical level [28]. As a result of the synergistic effect of the physical and chemical connections, the interfacial impedance of the battery is almost invariable after cycling. Li^+ transport at the PEO-SPE and PAN-SPE interfaces is achieved through the synergistic effect of cyano repulsion and ether attraction. This special Li^+ conducting mechanism in DLPE provides uniform Li^+ flux and fast Li^+ conduction, which results in stable electrolyte/electrode interfaces. The coulombic efficiency of a $LiFePO_4$/DLPE/Li battery was shown to be 99.5% after 130 cycles, showing superior cycling stability. With the DLPE incorporated in a $LiNi_{0.6}Co_{0.2}Mn_{0.2}O_2$ battery, a capacity of 176.0 mAh g^{-1} was achieved between 2.8 V to 4.3 V, with the coulombic efficiency remaining around 95% after 100 cycles.

2. Results and Discussion

2.1. Li Ion Transportation Mechanism in DLPE

To construct an SSE that would be compatible with both the Li anode and the high voltage cathode, double-layer polymer electrolytes were designed and combined into a whole. The DLPE consisted of two layers, a PEO-based solid polymer electrolyte (PEO-SPE) and a PAN-based solid polymer electrolyte (PAN-SPE). As shown in Figure 1a, the PAN-SPE precursor was scraped on a prepared cathode and dried in a vacuum oven. Then, the PEO-SPE precursor was covered on the PAN-SPE, dried in the vacuum oven and photocured under an ultraviolet (UV) lamp. This in situ manufacture method can minimize the interfacial impedance between membranes and contribute to faster Li ion transport at the electrolyte-electrolyte interface (Figure S1). More intriguingly, once PEO contacts with PAN, the hydroxy group of PEO-SPE can form an O-H⁻N hydrogen bond with the cyano group in PAN-SPE (Figure 1b), which connects the two layers of DLPE at a chemical microscopic level. Both the physical and chemical connections contribute to faster Li ion transport at the electrolyte/electrolyte interface. In addition, the solvents in the electrolyte manufacturing process are different. It was found that PEO was soluble in acetonitrile and PAN was soluble in N,N-dimethyl formamide (DMF), but PAN was almost insoluble in acetonitrile (Figure S2). Given this, PAN aggregated on one side, and PEO entirely aggregated on the other side, ensuring good interfacial contact, while avoiding interpenetration between the two layers. The interfacial resistance of the PAN-SPE battery

was large, but the introduction of PEO-SPE increased compatibility with the electrode (Figure S3). As a result of the in situ synthesis method, the interfacial resistance of the DLPE battery was smaller than that of the PAN-SPE and PEO-SPE stacked together (PAN-SPE/PEO-SPE) batteries (Figure 1c,d). The impedance of PAN-SPE/PEO-SPE battery cycles increased greatly from 1 to 50 cycles, which delivered poor cycle stability. However, the impedance of DLPE was almost stable after 10 cycles because of the close interfacial contact.
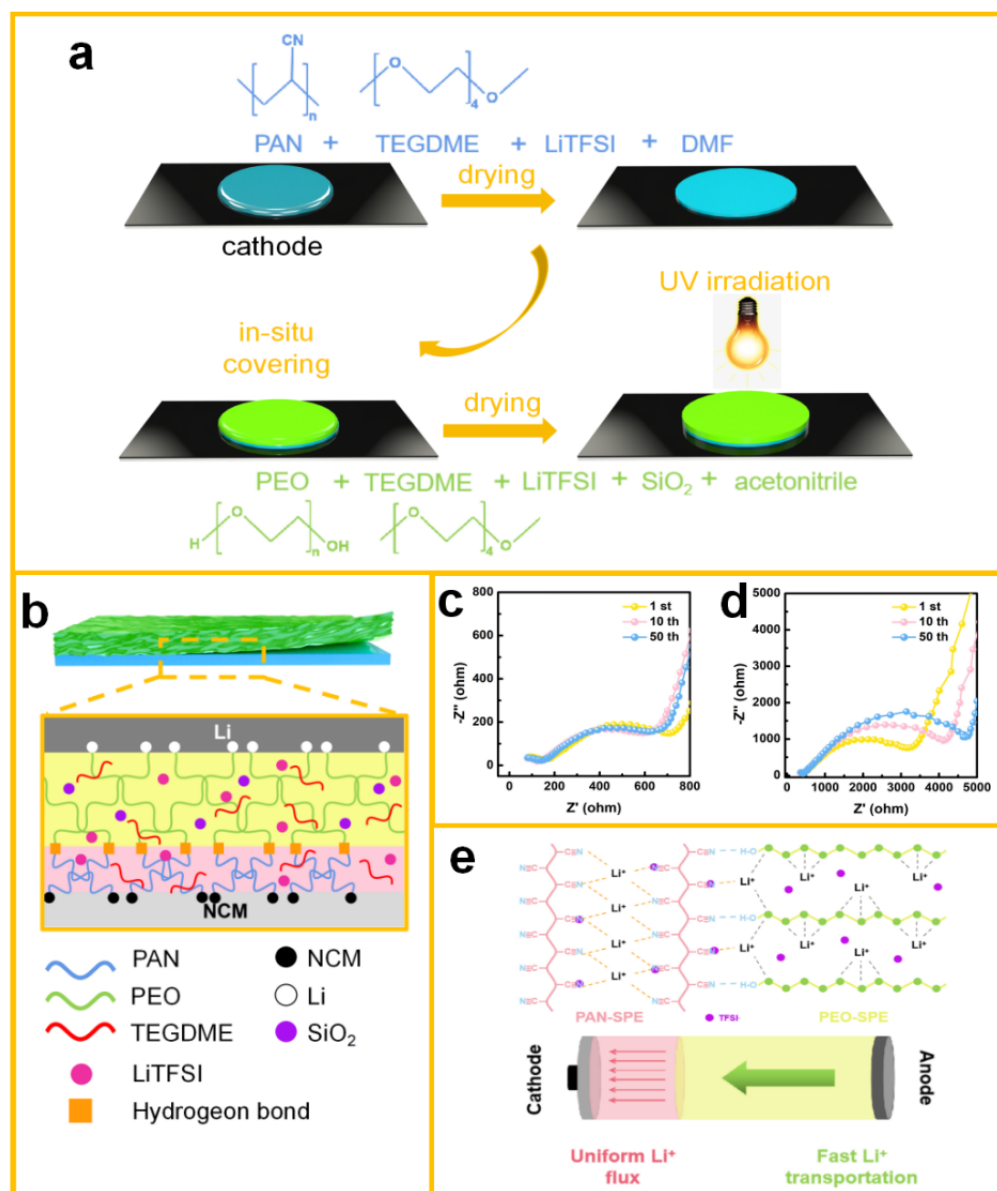

Figure 1. (**a**) Schematic illustration of DLPE membrane preparation, (**b**) structure diagram of DLPE; Nyquist plots of the interfacial resistance after 50 cycles for (**c**) DLPE battery and (**d**) PAN-SPE/PEO-SPE battery, (**e**) the mechanism of Li$^+$ conduction in DLPE.

Figure 1e demonstrates the Li ion transport between the two-layer electrolyte and the electrolyte-electrolyte interface. In PEO-SPE, PEO is cross-linked with Tetraethylene glycol dimethyl ether (TEGDME) to form a three-dimensional network structure, which disrupts the structure of PEO, expands the region of the amorphous phase, and accelerates the extent of PEO chain segment motion. The ether group of TEGDME can not only dissociate LiTFSI into Li$^+$ and TFSI$^-$, but also has a weak interaction with Li$^+$, which facilitates fast Li$^+$ transportation in PEO-SPE. Compared with the transport mechanism of PEO, in PAN-SPE,

the functional cyano group of PAN becomes an electron-withdrawing group due to the conjugation effect, which not only repels Li^+, but also fixes $TFSI^-$. During the movement of the PAN segments, most of the anions are bounded by $-C\equiv N$, and Li^+ is continuously pushed by $-C\equiv N$ under the action of the electric field, which regulates Li^+ transport and facilitates uniform Li deposition [29]. However, high crystallinity limits the transport of long PAN chains, and the introduction of TEGDME solves this problem [30]. TEGDME is uniformly distributed between the PAN chains, which reduces the intermolecular forces and provides more free volume for the chains to conduct Li^+ dissociation, resulting in a higher Li^+ transport rate. At the interface, Li^+ transport at the PEO-SPE and PAN-SPE interfaces is achieved through the synergistic effect of cyano repulsion and ether attraction.

2.2. Characteristics of DLPE

Scanning electron microscope (SEM) and energy dispersive spectroscopy (EDS) mappings were used to confirm the double-layer structure. As presented in the cross-section (Figure 2b), the thicknesses of PEO-SPE and PAN-SPE were 28 and 17 µm, respectively. The total thickness of the DLPE was around 45 µm—relatively thin among double-layer electrolytes that have been reported. The EDS mappings (Figures 2e–h and S4) clearly illustrate the double-layer structure of the electrolyte and the homogeneous material distribution in each layer. Furthermore, the electrolyte exhibits a Janus structure, which has excellent flexibility. (Figure 2a). One side of the DLPE was irregular, and the other side was smooth. The difference in the surface depended on the physical characteristic of PEO and PAN. The SEM of PEO-SPE showed a wrinkled texture (Figure 2c), which is the typical structure of cross-linked polymers. These wrinkles were evenly distributed throughout the PEO-SPE, causing the surface to be not smooth. In contrast, there was a smooth and flat surface without any crystallized phase in the SEM image of PAN-SPE (Figure 2d), which demonstrated that the structure was extremely dense.
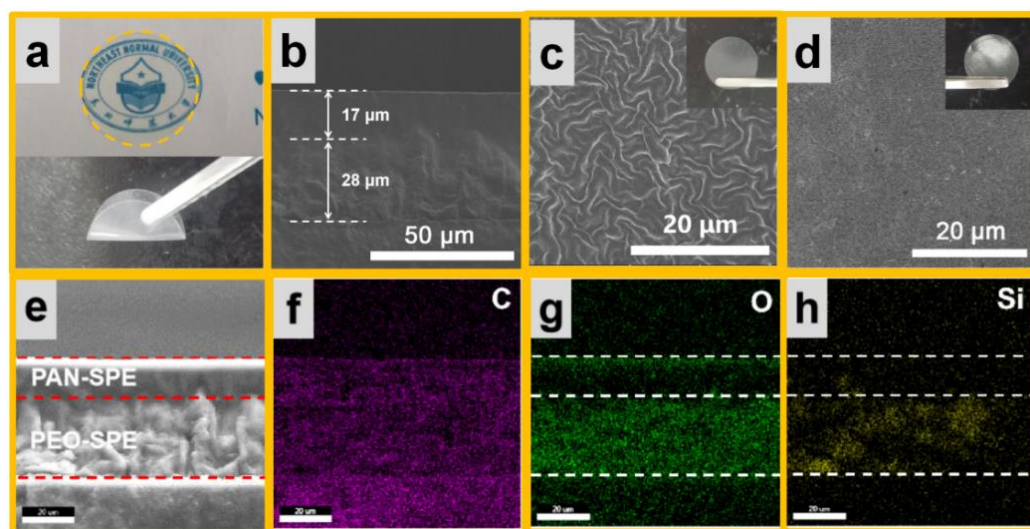
Figure 2. (**a**) Optical photograph of DLPE membrane. (**b**) SEM image of the cross-section of DLPE membrane. SEM images of the surface of (**c**) PEO-SPE and (**d**) PAN-SPE membranes. (**e–h**) EDS mappings of the cross-section of DLPE membrane.

The results of X-ray diffraction (XRD) show the crystallinity changes of the SPEs (Figure 3a). Compared with pure PEO, the diffraction peaks of PEO-SPE from 19° to 24° were weakened and broadened. This is because the addition of TEGDME caused cross-linking with PEO, which increase the amorphous region. Simultaneously, SiO_2 further disturbed the ordered structure and reduced the high crystallinity of PEO to some extent. However, the diffraction peak of SiO_2 was relatively weak, indicating the number of SiO_2 molecules exposed to the surface of electrolyte were very few. In addition, the sharp

peak of pure PAN in 17° disappeared, replaced by the smooth peak of PAN-SPE. This was due to the introduction of TEGDME. As a plasticizer, TEGDME occupies space in PAN long chains, which gives PAN chains larger free volume in which to maneuver. Naturally, the increase in the amorphous region increased the ionic conductivity and benefitted the electrochemical properties of PAN-SPE, matching closely the results for the ionic conductivity. In consequence, the ionic conductivity of PAN solid electrolyte increased from 2.5×10^{-17} S cm^{-1} to 2×10^{-6} S cm^{-1} (Figure S5). Tensile strength measurements were carried out to test the mechanical properties of PEO-SPE, PAN-SPE and DLPE. As illustrated in Figure 3b, the maximal tensile strength and strain of PEO-SPE were 0.8 MPa and 38%, respectively. The corresponding characteristics of PAN-SPE were 12.7 MPa and 3.8%, respectively. High tensile strength can slow down the kinetics of deposition and inhibit dendrite propagation, and high tensile strain is beneficial to the assembly of batteries. Nevertheless, neither PEO-SPE nor PAN-SPE were perfect. The DLPE neutralized their shortcomings, with maximal tensile strength and strain of 1.96 MPa and 10%, respectively. The structure of DLPE was mechanically strong enough to reduce the formation of the dendrite nuclei and to facilitate the process of batteries assembly. Thermo-gravimetric analysis (TGA) was used to study the thermal decomposition and stability of electrolytes. The TGA curves of DLPE were stable until 125 °C (Figure 3c), which indicated that all the electrolytes could meet most of the working temperature requirements of lithium-ion batteries. The weight loss at 125 °C of PAN-SPE was due to the evaporation of TEGDME. The weight loss at 125 °C of DLPE and PEO-SPE was due to the degradation of TEGDME and PEO which were not cross-linked (Figure S6). The weight loss at 350 °C was mainly due to the decomposition of the cross-linked PEO-SPE. However, DLPE evidenced a 14% weight loss at 350 °C, which was less than PEO-SPE. This was because PAN-SPE has high thermal stability, with 55 % weight retention observed at 700 °C. In consequence, the introduction of PAN-SPE improved the thermal stability of DLPE compared to that that of PEO-SPE.
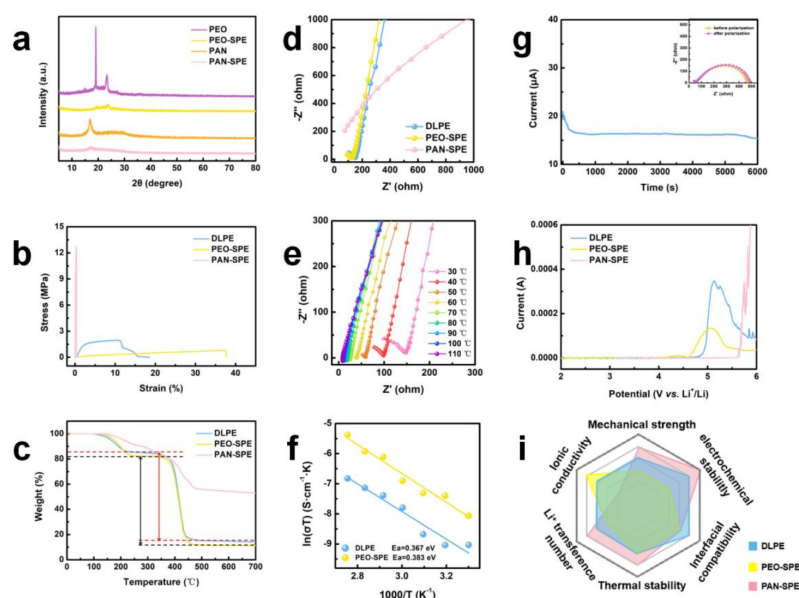
Figure 3. (**a**) XRD patterns of pure PEO, PEO-SPE membrane, pure PAN and PAN-SPE membranes. (**b**) Stress-strain curves of DLPE, PEO-SPE and PAN-SPE membranes. (**c**) TGA curves of DLPE, PEO-SPE and PAN-SPE membranes. (**d**) EIS curves of DLPE, PEO-SPE and PAN-SPE membranes. (**e**) EIS analysis and (**f**) Arrhenius linear fitting plots of the DLPE at various temperatures. (**g**) AC curve and impedance spectra before and after polarization. (**h**) linear sweep voltammetry (LSV) curves of DLPE, PEO-SPE and PAN-SPE. (**i**) Radar plots that compare the performance of DLPE, PEO-SPE and PAN-SPE.

Ionic conductivity is one of the important indexes by which to measure SSEs. Although PAN possesses numerous excellent physical characteristics, a pure PAN electrolyte cannot charge and discharge normally. Despite addition of plasticizer, the ionic conductivity of PAN-SPE was still not high enough, resulting in low battery capacity. For this reason, PEO-SPE with an ionic conductivity of 9.5×10^{-5} S cm^{-1} was used to combine with PAN-SPE with a conductivity of 2×10^{-6} S cm^{-1}. As a result, the obtained DLPE had an ionic conductivity of 3.8×10^{-5} S cm^{-1} at ambient temperature (Figure 3d). Although use of DLPE requires some concessions with respect to ionic conductivity, it improved other electrochemical and physical properties. In addition, the ionic conductivity of DLPE at different temperatures demonstrated that the electrolyte can бoperate normally in a range of 30–110 °C, which is consistent with the results of TGA (Figure 3e). Generally, the migration process of Li$^+$ in SSB can be divided into two steps: the dissociation of lithium salts and the diffusion of Li$^+$ in electrolytes [31,32]. Due to the high dielectric constant of TEGDME, which can achieve effective separation of anion-cation pairs in electrolytes, the dissociation of lithium salts is not key to the migration of Li$^+$. The migration of Li$^+$ along polymer chains is the rate-determining step, which needs to overcome energy barriers. The activation energy (Ea) of DLPE and PEO-SPE for ion transfer can be calculated by the slope of the line in Figure 3f and the Arrhenius equation. The Arrhenius equation,

$$\sigma T = A \exp\left(-\frac{Ea}{K_B T}\right)$$

where σ is the ionic conductivity, T is the absolute temperature, K$_B$ is the Boltzmann constant, A is the pre-exponential constant, and the Ea is the activation energy. The Ea values upon Li$^+$ transfer in electrolytes were calculated to be 0.367 eV and 0.383 eV for DLPE and PEO-SPE, respectively. DLPE had a lower migration barrier for ion transport than PEO-SPE, owing to the unique Li$^+$ transport pathway in PAN-SPE. It is well-known that the cyano group is a strong electron-sucking group that can immobilize anions effectively. Li$^+$ could transfer uniformly in PAN-SPE without considering the influence of TFSI$^-$, which caused the high Li$^+$ transference number of 0.64 for PAN-SPE (Figure S7a). However, PEO-SPE had a low Li$^+$ transference number (~0.20) (Figure S7b). So, as the middle ground, the Li$^+$ transference number of DLPE was ~0.41 (Figure 3g). The linear sweep voltammetry (LSV) curves of DLPE, PEO-SPE and PAN-SPE were measured to test the electrochemical stability window. To match the NCM cathode materials, the operating voltage range of lithium-ion batteries is 3–4.5 V (vs. Li/Li$^+$). This requires that the solid polymer electrolytes can ensure normal and stable operation of the batteries within the electrochemical stability window. In Figure 3h, for the PAN-SPE, the LSV curve remained stable until 5.6 V; so PAN-SPE would not decompose under 5.6 V. However, the LSV curve of PEO-SPE showed fluctuation at 4.2 V, which can be interpreted in terms of the decomposition of PEO-SPE during the oxidation process. To achieve a balance, a wide electrochemical stability window of 0–4.8 V can be derived from the LSV curve of DLPE, which indicates that the heterogeneous double-layer design can play a vital role in high voltage electrolytes. In summary, the DLPE possesses high ionic conductivity, high Li$^+$ transference number, wide electrochemical stability window, good mechanical strength and thermal stability, superior in comparison with PEO-SPE and PAN-SPE (Figure 3i).

2.3. Interfacial Compatibility of DLPE and Li Anode

The long-term electrochemical compatibility and stability with Li metal were measured by galvanostatic charge/discharge voltage profiles in symmetric Li batteries. The DLPE was sandwiched between two 0.6 mm Li foils. As shown in Figure 4a, from the very beginning, PAN-SPE had a polarization voltage of 0.13 V, and a short circuit after 195 h. Although the battery was recharged and discharged 12 h later, the polarization voltage increased, finally reaching 0.36 V and plummeting after 370 h, resulting in a short circuit. The voltage profile suggests that PAN-SPE reacted with Li metal continuously, which caused the huge polarization voltage, while the battery short circuit occurred finally as

the side reaction continued. In contrast, after the voltage was stable, the DLPE exhibited a relatively flat polarization voltage profile, with slightly decreased polarization voltage from 95 mV (200 h) to 85 mV (900 h). The results show that covering PEO-SPE, which has a low polarization voltage (Figure S8), on the side of PAN-SPE, could effectively reduce the side reactions.
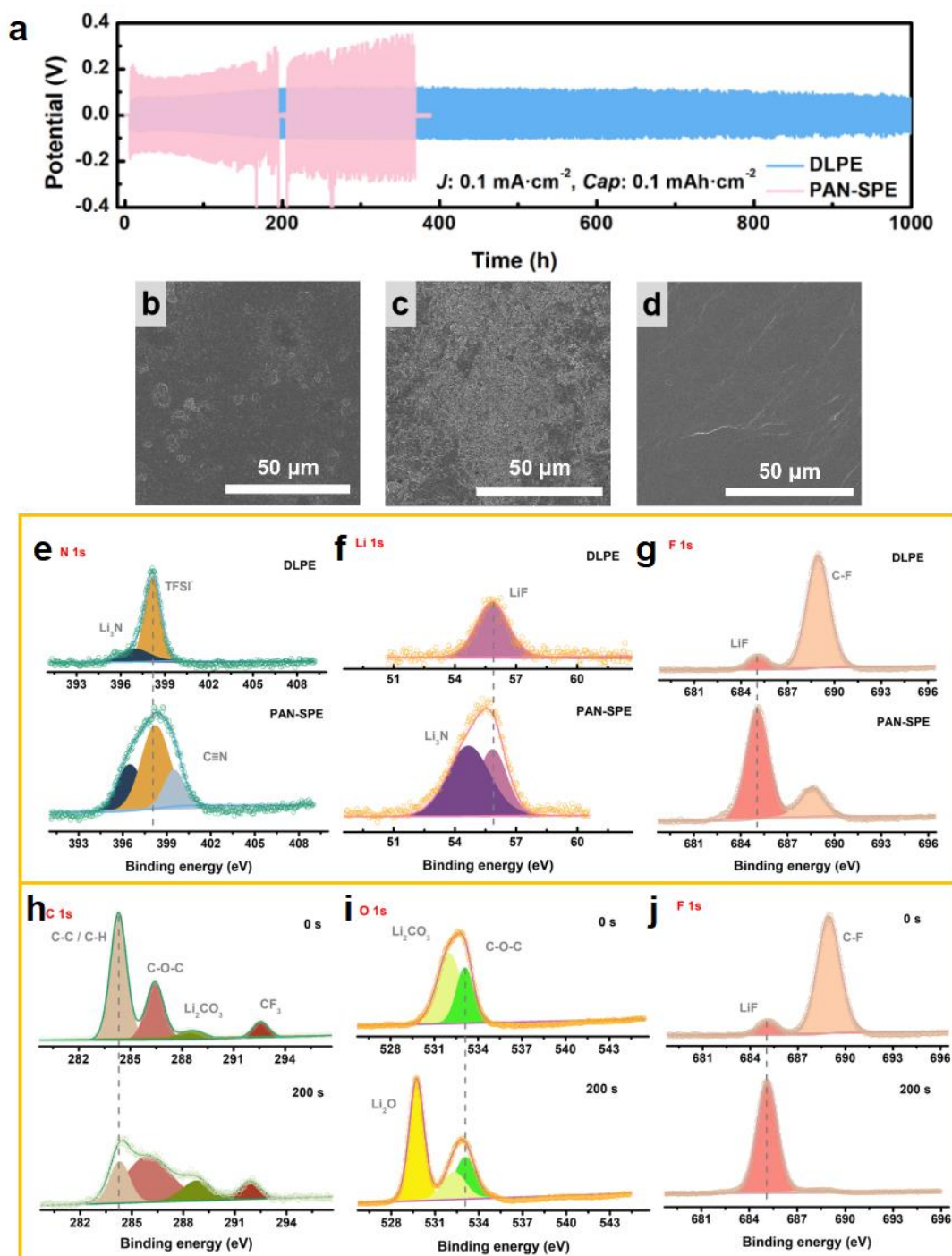
Figure 4. Voltage profiles of (**a**) Li/PAN-SPE/Li and Li/DLPE/Li symmetric batteries at a current density of 0.1 mA cm^{-2}. The corresponding SEM images at Li metal anode surface after 50 cycles (**b**) for DLPE; (**c**) for PAN-SPE. (**d**) SEM image of the surface of pure Li foil. (**e–g**) High-resolution XPS spectra of DLPE and PAN-SPE anode after 50 cycles. (**h–j**) High-resolution XPS spectra of DLPE anode after 50 cycles before and after sputtering for 200 s.

To observe the surface morphology of the Li metal anode, the DLPE battery and the PAN-SPE battery with 100 cycles were disassembled. As shown in Figure 4b, after 100 cycles, the Li anode of the DLPE battery achieved smooth deposition with metal luster, benefitting from the uniform Li$^+$ flux of PAN-SPE. In contrast, the surface of the Li metal anode from the PAN-SPE battery showed a lot of "dead lithium" and large voids caused by the "passivation effect" (Figure 4c), which is the reaction of the cyano group in PAN and the Li metal anode. As a strong polar group, the cyano group, with no constraint, can react with the active Li metal, forming a passivation layer on the surface of the Li anode. This passivation layer has a huge impedance and thickens as the charging and discharging occurs, which hinders the transport of Li$^+$. The passivation effect attenuates the capacity of batteries. Exposing the PEO-SPE side of the DLPE to the Li anode solved this problem perfectly.

In addition, compared with the surface of pure Li (Figure 4d), there was a passivation layer on the surface of the DLPE anode, which had a thin solid electrolyte interphase (SEI) layer. The characteristics of the formed SEI layer are known to be related to its chemical composition, which was further analyzed by X-ray photoelectron spectroscopy (XPS). PEO-SPE contacts with the anode, which can form stable SEI on the anode (Figure S9), so we chose PAN-SPE as the comparison sample. Figure 4e–g shows the high-resolution XPS spectra of the DLPE battery and the PAN-SPE battery after 100 cycles, which are the spectra for N 1s, Li 1s and F 1s, respectively. As shown in the spectra, the SEI of the DLPE battery mostly consisted of Li$_3$N and LiF. Li$_3$N and LiF are known as superior Li$^+$ conductors and can provide fast Li$^+$ transport and uniform Li$^+$ flux [33,34]. In the N 1s XPS spectra of PAN-SPE (Figure 4e), the peak, located at ~399.5 eV, was attributed to the -C≡N on the surface of the Li anode. The cyano group of PAN obtained electrons during the charge-discharge process, and reacted with the Li anode, resulting in an increase in battery internal resistance and capacity loss. To prevent direct contact between PAN and Li, the design of the double-layer DLPE has advantages. Due to the existence of ethers, the SEI layer has a dual-layer structure [35]. As shown in the C 1s XPS spectrum (Figure 4h), the intensify of C-C (~284.6 eV, C 1s), as the skeleton of the polymers, declined after sputtering, indicating the polymer content in the outer layer of SEI was higher than that of the inner layer. A new Li$_2$O peak at 531.0 eV in the O 1s spectrum appeared, which originated from the reaction between the -C-O-C- group in the polymer and the Li metal. It was determined that the inner layer of SEI was inorganic oxide Li$_2$O, and the outer layer of SEI was organic polymer with C-O-C. In addition, as shown in the F 1s spectra (Figure 4j), the content of LiF sharply increased, indicating that the composition of SEI had a large number of LiF molecules apart from Li$_2$O. The hard inner layer of SEI had high mechanical strength, which could effectively inhibit the formation of lithium dendrite crystal nuclei and make lithium deposition more uniform, while the soft SEI outer layer could adapt to the deformation of the lithium metal anode during the Li ion stripping/depositing process. As a result, LMBs with DLPE showed a stable SEI and had excellent electrochemical performance.

2.4. Interfacial Compatibility of DLPE and Cathode

The batteries were assembled to evaluate their electrochemical performance. To demonstrate the practicality of DLPE in Li metal batteries, an LiFePO$_4$ (LFP)/DLPE/Li battery was assembled and tested. Figure 5a shows the cycle performance of DLPE batteries at a rate of 0.2 C at 30 °C. The specific discharge capacity of DLPE battery after activation at 0.2 C was 148.1 mAh g^{-1}, with 98.8% retention after 130 cycles. The coulombic efficiency remained above 99.5% from beginning to end, verifying excellent electrochemical stability. In addition, the LiNi$_{0.6}$Co$_{0.2}$Mn$_{0.2}$O$_2$ (NCM622)/DLPE/Li and NCM622/PEO-SPE/Li batteries were assembled to test their electrochemical performance under high voltage. As shown in Figure 5b, the specific discharge capacity of the DLPE battery at 0.1 C between 2.8 V to 4.3 V was 176.0 mAh g^{-1}, and the coulombic efficiency remained around 95% after 100 cycles. Conversely, batteries with PEO-SPE could not maintain stable charge and discharge and their coulombic efficiency attenuated rapidly after 50 cycles. This was

ascribed to the fact that the PEO-based solid electrolyte was intolerant to high voltage and had a low Li^+ transference number. These features caused great damage at the electrode-electrolyte interfaces. The side reaction led to the decomposition of the electrolyte and the intense accumulation of the electric double layer [36]. The introduction of PAN-SPE immobilized anions of lithium salts, reducing the concentration gradient and forming a stable cathode electrolyte interphase (CEI) [37].
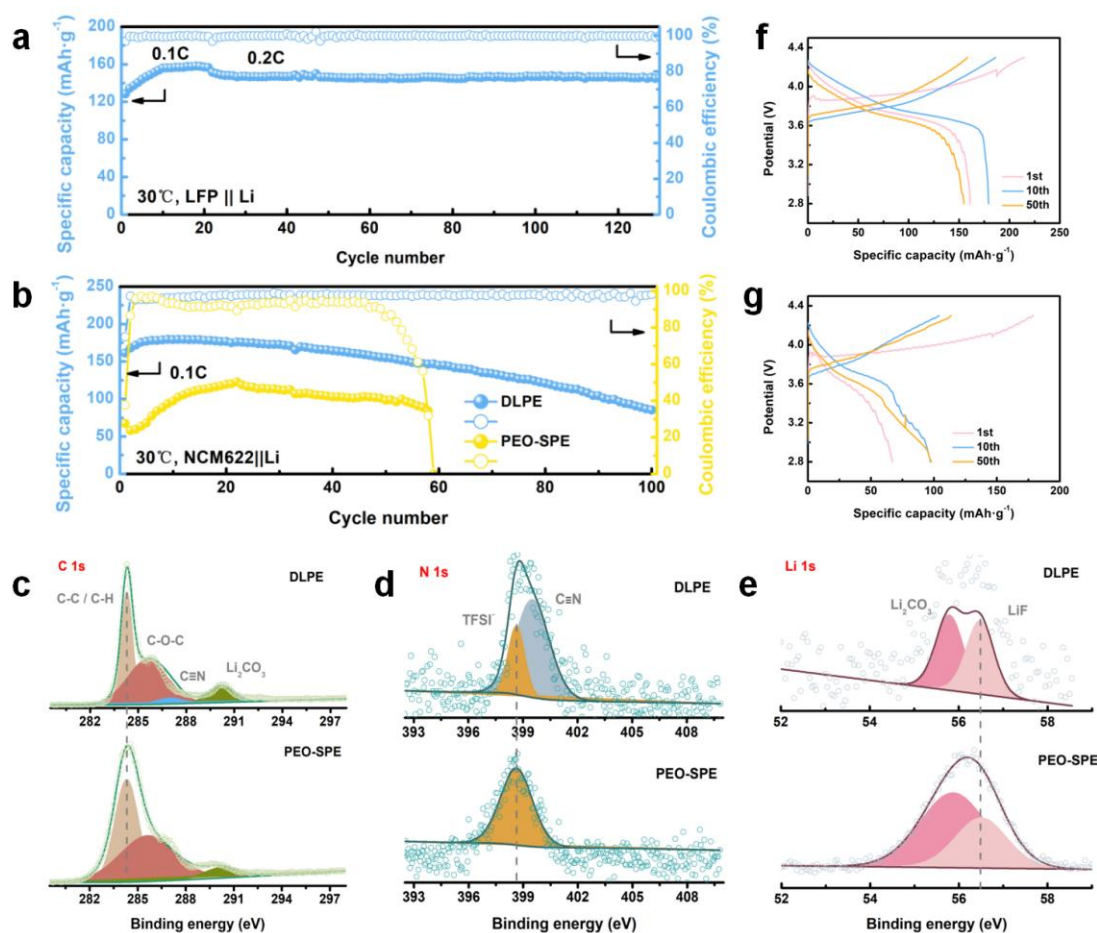
Figure 5. (**a**) Electrochemical performance of LFP//Li using DLPE. (**b**) Electrochemical performance of NCM622//Li using DLPE and PEO-SPE. (**c–e**) High-resolution XPS spectra of DLPE and PEO-SPE cathode after 50 cycles. Charge-discharge curves of NCM622//Li with different cycles assembled by (**f**) DLPE and (**g**) PEO-SPE at 0.1 C.

XPS was carried out to explore the composition of CEI. It has been mentioned that PEO could be oxidized when contacting the transition metal oxide cathode, and would produce as a by-product, Li_2CO_3, increasing the thickness of the CEI during charging and discharging and accelerating the decline in battery capacity. As shown in Figure 5e, the constituents of CEI on the surface of PEO-SPE battery after 100 cycles were Li_2CO_3 and LiF. In contrast, LiF made up the majority constituent of the CEI of the DLPE battery after sputtering (Figure S10), which was beneficial to the rapid transfer of Li^+ and forming of a stable CEI [38]. This was attributed to the preferential interaction of the cyano group and NCM622 cathode, which was confirmed by the appearance of -C≡N in Figure 5c (~286.7 eV, C 1s) and Figure 5d (~399.5 eV, N 1s). The CEI with abundant LiF could provide efficient Li^+ diffusion channels, leading to a lower polarization of the DLPE batteries than that of the PEO-SPE batteries (Figure 5f,g). The internal resistance of the DLPE batteries increased slightly after 50 cycles because the PAN-SPE blocked direct contact between PEO and the

cathode and the EO segments could not be decomposed which controlled the thickening of CEI.

3. Conclusions

In this study, we designed a DLPE with PEO-SPE contacting the anode and PAN-SPE contacting the cathode for high-performance Li metal batteries. DLPE exhibited a wide electrochemical stability window (0–4.8 V) and an excellent Li^+ transference number (~0.4). An LFP/DLPE/Li battery exhibited superb cycle performance, with coulombic efficiency remaining above 99.5% after 130 cycles at 30 °C. Moreover, the specific discharge capacity of an NCM622/DLPE/Li battery was 176.0 mAh g^{-1} at 4.3 V, and the coulombic efficiency remained around 95 % after 100 cycles. This design of double-layer electrolytes offers an ideal strategy to solve the interfacial problem of high-energy-density Li metal batteries.

Supplementary Materials: The following are available online at https://www.mdpi.com/article/10.3390/inorganics10040042/s1, Figure S1: Optic photos of DLPE by in situ two-step method; Figure S2: Photos of PAN dissolution in ACN and DMF; Figure S3: The Nyquist plot of NCM622/DLPE/Li, NCM622/PEO-SPE/Li and NCM622/PAN-SPE/; Figure S4: LiThe EDS mapping of N element for the DLPE membrane; Figure S5: (a) The Nyquist plot of PAN and PAN-SPE, (b) the initial of the Nyquist plot; Figure S6: TGA curves of pure PEO; Figure S7: AC curve and impedance spectra before and after polarization of (a) PAN-SPE and (b) PEO-SPE; Figure S8: Voltage profiles of the Li/PEO-SPE/Li symmetric batteries at a current density of 0.1 mA cm^{-2}; Figure S9: (a–c) High-resolution XPS spectra of DLPE and PEO-SPE anode after 50 cycles; Figure S10: High-resolution XPS spectra of (a) PEO-SPE and (b) DLPE cathode after 50 cycles before and after sputtering for 200 s.

References

1. Fan, L.; Wei, S.; Li, S.; Li, Q.; Lu, Y. Recent Progress of the Solid-State Electrolytes for High-Energy Metal-Based Batteries. *Adv. Energy Mater.* **2018**, *8*, 1702657. [CrossRef]
2. Chen, Z.; Chen, W.; Wang, H.; Zhang, C.; Qi, X.; Qie, L.; Wu, F.; Wang, L.; Yu, F. Lithiophilic anchor points enabling endogenous symbiotic Li3N interface for homogeneous and stable lithium electrodeposition. *Nano Energy* **2022**, *93*, 106836. [CrossRef]
3. Li, W.; Rao, S.; Xiao, Y.; Gao, Z.; Chen, Y.; Wang, H.; Ouyang, M. Fire boundaries of lithium-ion cell eruption gases caused by thermal runaway. *iScience* **2021**, *24*, 102401. [CrossRef]
4. Zhang, R.; Shen, X.; Zhang, Y.T.; Zhong, X.L.; Ju, H.T.; Huang, T.X.; Chen, X.; Zhang, J.D.; Huang, J.Q. Dead lithium formation in lithium metal batteries: A phase field model. *J. Energy Chem.* **2021**. [CrossRef]
5. Zhang, S.; Ueno, K.; Dokko, K.; Watanabe, M. Recent Advances in Electrolytes for Lithium-Sulfur Batteries. *Adv. Energy Mater.* **2015**, *5*, 1500117. [CrossRef]
6. Zhao, T.; Li, S.; Liu, F.; Wang, Z.; Wang, H.; Liu, Y.; Tang, X.; Bai, M.; Zhang, M.; Ma, Y. Molten-Li infusion of ultra-thin interfacial modification layer towards the highly-reversible, energy-dense metallic batteries. *Energy Storage Mater.* **2022**, *45*, 796–804. [CrossRef]

7. Ren, X.; Zou, L.; Cao, X.; Engelhard, M.H.; Liu, W.; Burton, S.D.; Lee, H.; Niu, C.; Matthews, B.E.; Zhu, Z.; et al. Enabling High-Voltage Lithium-Metal Batteries under Practical Conditions. *Joule* **2019**, *3*, 1662–1676. [CrossRef]

8. Lee, K.; Han, S.; Lee, J.; Lee, S.; Kim, J.; Ko, Y.; Kim, S.; Yoon, K.; Song, J.H.; Noh, J.H.; et al. Multifunctional Interface for High-Rate and Long-Durable Garnet-Type Solid Electrolyte in Lithium Metal Batteries. *ACS Energy Lett.* **2021**, *7*, 381–389. [CrossRef]

9. Ma, Z.; Chen, J.; Vatamanu, J.; Borodin, O.; Bedrov, D.; Zhou, X.; Zhang, W.; Li, W.; Xu, K.; Xing, L. Expanding the low-temperature and high-voltage limits of aqueous lithium-ion battery. *Energy Storage Mater.* **2022**, *45*, 903–910. [CrossRef]

10. Wang, M.; Wang, J.; Si, J.; Chen, F.; Cao, K.; Chen, C. Bifunctional composite separator with redistributor and anion absorber for dendrites-free and fast-charging lithium metal batteries. *Chem. Eng. J.* **2022**, *430*, 132971. [CrossRef]

11. Liu, F.; Xu, R.; Wu, Y.; Boyle, D.T.; Yang, A.; Xu, J.; Zhu, Y.; Ye, Y.; Yu, Z.; Zhang, Z.; et al. Dynamic spatial progression of isolated lithium during battery operations. *Nature* **2021**, *600*, 659–663. [CrossRef]

12. Fu, F.; Lu, W.; Zheng, Y.; Chen, K.; Sun, C.; Cong, L.; Liu, Y.; Xie, H.; Sun, L. Regulating lithium deposition via bifunctional regular-random cross-linking network solid polymer electrolyte for Li metal batteries. *J. Power Sources* **2021**, *484*, 229186. [CrossRef]

13. Duan, H.; Fan, M.; Chen, W.P.; Li, J.Y.; Wang, P.F.; Wang, W.P.; Shi, J.L.; Yin, Y.X.; Wan, L.J.; Guo, Y.G. Extended Electrochemical Window of Solid Electrolytes via Heterogeneous Multilayered Structure for High-Voltage Lithium Metal Batteries. *Adv. Mater.* **2019**, *31*, e1807789. [CrossRef] [PubMed]

14. Dastafkan, K.; Wang, S.; Rong, C.; Meyer, Q.; Li, Y.; Zhang, Q.; Zhao, C. Cosynergistic Molybdate Oxo-Anionic Modification of FeNi-Based Electrocatalysts for Efficient Oxygen Evolution Reaction. *Adv. Funct. Mater.* **2021**, *32*, 2107342. [CrossRef]

15. Lu, J.; Zhou, J.; Chen, R.; Fang, F.; Nie, K.; Qi, W.; Zhang, J.N.; Yang, R.; Yu, X.; Li, H.; et al. 4.2 V poly(ethylene oxide)-based all-solid-state lithium batteries with superior cycle and safety performance. *Energy Storage Mater.* **2020**, *32*, 191–198. [CrossRef]

16. Ma, Y.; Sun, Q.; Wang, S.; Zhou, Y.; Song, D.; Zhang, H.; Shi, X.; Zhang, L. Li salt initiated in-situ polymerized solid polymer electrolyte: New insights via in-situ electrochemical impedance spectroscopy. *Chem. Eng. J.* **2022**, *429*, 132483. [CrossRef]

17. Chen, L.; Li, Y.; Li, S.P.; Fan, L.Z.; Nan, C.W.; Goodenough, J.B. PEO/garnet composite electrolytes for solid-state lithium batteries: From "ceramic-in-polymer" to "polymer-in-ceramic". *Nano Energy* **2018**, *46*, 176–184. [CrossRef]

18. Yuan, H.; Luan, J.; Yang, Z.; Zhang, J.; Wu, Y.; Lu, Z.; Liu, H. Single Lithium-Ion Conducting Solid Polymer Electrolyte with Superior Electrochemical Stability and Interfacial Compatibility for Solid-State Lithium Metal Batteries. *ACS Appl. Mater. Interfaces* **2020**, *12*, 7249–7256. [CrossRef]

19. Yang, Z.; Yuan, H.; Zhou, C.; Wu, Y.; Tang, W.; Sang, S.; Liu, H. Facile interfacial adhesion enabled LATP-based solid-state lithium metal battery. *Chem. Eng. J.* **2020**, *392*, 123650. [CrossRef]

20. Wan, Z.; Lei, D.; Yang, W.; Liu, C.; Shi, K.; Hao, X.; Shen, L.; Lv, W.; Li, B.; Yang, Q.H.; et al. Low Resistance-Integrated All-Solid-State Battery Achieved by Li7La3Zr2O12 Nanowire Upgrading Polyethylene Oxide (PEO) Composite Electrolyte and PEO Cathode Binder. *Adv. Funct. Mater.* **2019**, *29*, 1805301. [CrossRef]

21. Nie, K.; Wang, X.; Qiu, J.; Wang, Y.; Yang, Q.; Xu, J.; Yu, X.; Li, H.; Huang, X.; Chen, L. Increasing Poly(ethylene oxide) Stability to 4.5 V by Surface Coating of the Cathode. *ACS Energy Lett.* **2020**, *5*, 826–832. [CrossRef]

22. Zhang, J.; Wang, P.F.; Bai, P.; Wan, H.; Liu, S.; Hou, S.; Pu, X.; Xia, J.; Zhang, W.; Wang, Z.; et al. Interfacial Design for a 4.6 V High-Voltage Single-Crystalline LiCoO2 Cathode. *Adv. Mater.* **2022**, *34*, e2108353. [CrossRef] [PubMed]

23. Yoon, T.; Soon, J.; Lee, T.J.; Ryu, J.H.; Oh, S.M. Dissolution of cathode-electrolyte interphase deposited on LiNi0.5Mn1.5O4 for lithium-ion batteries. *J. Power Sources* **2021**, *503*, 230051. [CrossRef]

24. Liang, J.Y.; Zeng, X.X.; Zhang, X.D.; Zuo, T.T.; Yan, M.; Yin, Y.X.; Shi, J.L.; Wu, X.W.; Guo, Y.G.; Wan, L.J. Engineering Janus Interfaces of Ceramic Electrolyte via Distinct Functional Polymers for Stable High-Voltage Li-Metal Batteries. *J. Am. Chem. Soc.* **2019**, *141*, 9165–9169. [CrossRef]

25. Cao, Z.; Zheng, X.; Wang, Y.; Huang, W.; Li, Y.; Huang, Y.; Zheng, H. Tailoring a multifunctional, boron and fluoride-enriched solid-electrolyte interphase precursor towards high-rate and stable-cycling silicon anodes. *Nano Energy* **2022**, *93*, 106811. [CrossRef]

26. Ma, L.; Chen, S.; Li, N.; Liu, Z.; Tang, Z.; Zapien, J.A.; Chen, S.; Fan, J.; Zhi, C. Hydrogen-Free and Dendrite-Free All-Solid-State Zn-Ion Batteries. *Adv. Mater.* **2020**, *32*, e1908121. [CrossRef]

27. Song, H.; Sun, Y.; Zhu, J.; Xu, J.; Zhang, C.; Liu, T. Hydrogen-bonded network enables polyelectrolyte complex hydrogels with high stretchability, excellent fatigue resistance and self-healability for human motion detection. *Compos. Part B Eng.* **2021**, *217*, 108901. [CrossRef]

28. Wang, X.; Hao, X.; Xia, Y.; Liang, Y.; Xia, X.; Tu, J. A polyacrylonitrile (PAN)-based double-layer multifunctional gel polymer electrolyte for lithium-sulfur batteries. *J. Membr. Sci.* **2019**, *582*, 37–47. [CrossRef]

29. Pham, M.N.; Subramani, R.; Lin, Y.H.; Lee, Y.L.; Jan, J.S.; Chiu, C.C.; Teng, H. Acylamino-functionalized crosslinker to synthesize all-solid-state polymer electrolytes for high-stability lithium batteries. *Chem. Eng. J.* **2022**, *430*, 132948. [CrossRef]

30. Jyothi, N.K.; Venkataratnam, K.K.; Murty, P.N.; Kumar, K.V. Preparation and characterization of PAN-KI complexed gel polymer electrolytes for solid-state battery applications. *Bull. Mater. Sci.* **2016**, *39*, 1047–1055. [CrossRef]

31. Zhang, S.J.; Yin, Z.W.; Wu, Z.Y.; Luo, D.; Hu, Y.Y.; You, J.H.; Zhang, B.; Li, K.X.; Yan, J.W.; Yang, X.R.; et al. Achievement of high-cyclability and high-voltage Li-metal batteries by heterogeneous SEI film with internal ionic conductivity/external electronic insulativity hybrid structure. *Energy Storage Mater.* **2021**, *40*, 337–346. [CrossRef]

32. Lu, W.; Sun, L.; Zhao, Y.; Wu, T.; Cong, L.; Liu, J.; Liu, Y.; Xie, H. Elongating the cycle life of lithium metal batteries in carbonate electrolyte with gradient solid electrolyte interphase layer. *Energy Storage Mater.* **2021**, *34*, 241–249. [CrossRef]

33. Zhang, W.; Wu, Q.; Huang, J.; Fan, L.; Shen, Z.; He, Y.; Feng, Q.; Zhu, G.; Lu, Y. Colossal Granular Lithium Deposits Enabled by the Grain-Coarsening Effect for High-Efficiency Lithium Metal Full Batteries. *Adv. Mater.* **2020**, *32*, e2001740. [CrossRef] [PubMed]
34. Xu, S.M.; Duan, H.; Shi, J.L.; Zuo, T.T.; Hu, X.C.; Lang, S.Y.; Yan, M.; Liang, J.Y.; Yang, Y.G.; Kong, Q.H.; et al. In situ fluorinated solid electrolyte interphase towards long-life lithium metal anodes. *Nano Res.* **2020**, *13*, 430–436. [CrossRef]
35. Ding, J.F.; Xu, R.; Yan, C.; Li, B.Q.; Yuan, H.; Huang, J.Q. A review on the failure and regulation of solid electrolyte interphase in lithium batteries. *J. Energy Chem.* **2021**, *59*, 306–319. [CrossRef]
36. Wen, K.; Tan, X.; Chen, T.; Chen, S.; Zhang, S. Fast Li-ion transport and uniform Li-ion flux enabled by a double-layered polymer electrolyte for high performance Li metal battery. *Energy Storage Mater.* **2020**, *32*, 55–64. [CrossRef]
37. Zhang, J.N.; Li, Q.; Wang, Y.; Zheng, J.; Yu, X.; Li, H. Dynamic evolution of cathode electrolyte interphase (CEI) on high voltage $LiCoO_2$ cathode and its interaction with Li anode. *Energy Storage Mater.* **2018**, *14*, 1–7. [CrossRef]
38. Zhao, J.; Liang, Y.; Zhang, X.; Zhang, Z.; Wang, E.; He, S.; Wang, B.; Han, Z.; Lu, J.; Amine, K.; et al. In Situ Construction of Uniform and Robust Cathode-Electrolyte Interphase for Li-Rich Layered Oxides. *Adv. Funct. Mater.* **2020**, *31*, 2009192. [CrossRef]